Search for pulsars and magnetars with the Pierre Auger surface detector

H. Schoorlemmer
HEN462

February 1, 2008

Contents

Chapter 1

Introduction

The first cosmic rays were detected in 1912 by Victor Hess while taking measurements of ionizing radiation in a balloon at an altitude of 5800 m. At this altitude, the ionization rate turned out to be four times higher than on ground level. Victor Hess called this additional radiation "Hohenstralung", the origin of which was under debate. In later experiments, Millikan concluded that ionizing radiation enters our atmosphere from above. Therefore he named it cosmic rays. Since then, almost one century of cosmic ray research has had a large impact on astrophysics and physics. For example, the pion, and its decay, were detected by a photographic plate that was exposed to cosmic rays.
Extensive measurements on the energy, the direction and the composition of the particles arriving at Earth have been performed. Most recently, the Pierre Auger observatory, located in the pampas in Argentina, just to the north of Malargüe, was designed to measure the cosmic rays with the highest energies ($> 10^{18}$ eV). In this energy region some of the most intriguing questions in cosmic ray physics need answering. Where do these high energy cosmic rays come from? Do we see the GZK-cut off? The GZK cut off is a cut off on the energy of particles that travel trough space due to interaction of high energy charged particles with the cosmic microwave background radiation [1][2].
When a cosmic ray particle enters our atmosphere it will collide with the atoms in the atmosphere. This collision produces secondary particles. Subsequently, these secondary particles interact with particles in the atmosphere creating more particles. In this way a shower of particles is produced. This shower travels through the atmosphere as a flat *pancake*. When the energy is high enough, this pancake of particles hits the surface of the Earth. Traveling through the atmosphere the shower of particles interacts with the atmospheric nitrogen. The excited nitrogen emits fluorescence light, which can be detected using sensitive telescopes.
Currently, the Pierre Auger observatory applies two different techniques to measure air showers: particle detection at the surface of the Earth and detection of the atmospheric fluorescence light. The fluorescence detectors (Figure 1.1) trace the shower development in the atmosphere. The total amount of light gives

Figure 1.1: Left: The fluorescence station Los Leones. Each station contains 6 fluorescence telescopes. Right: A fluorescence telescope, the hollow mirror focuses the light on a photon multiplier camera.

a measurement of the total energy. The altitude at which the shower has its maximum size contains

information on the mass of the primary cosmic ray particle. In total, the Pierre Auger Observatory has four fluorescence stations that which overlook the area in which the surface detector is placed.

The surface detector(Figure 1.2), once completed, will consist of 1600 water tanks and will cover an area

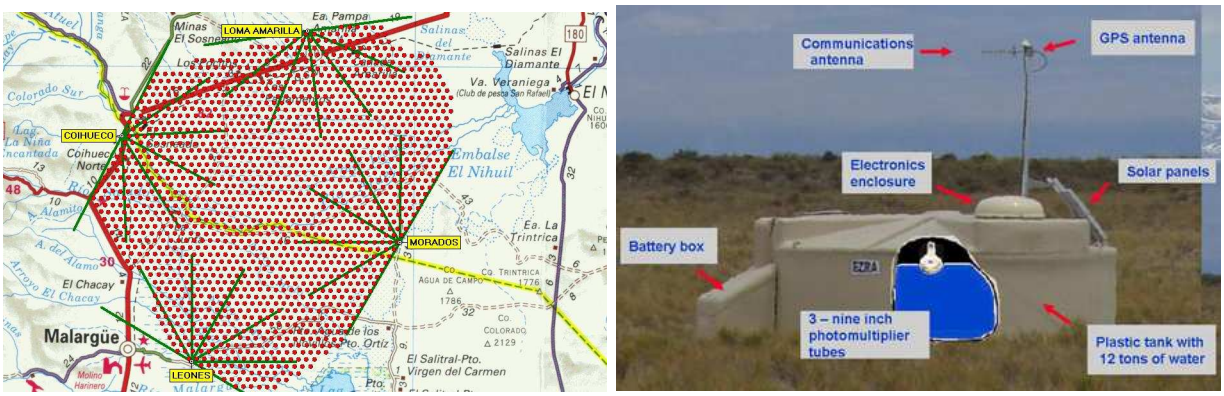

Figure 1.2: Left: The array of surface detectors, each red dot is one water tank. The four fluorescence stations are placed on the edges of the array. Right: One of the water tanks from the surface detector.

of about 3000 km^2. The distance from one tank to its nearest neighbor is 1.5 km. When charged particles go through the water in the tank, they travel faster than the speed of light in water. Therefore, Cerenkov radiation is emitted. This light is measured by photo-multiplier tubes in the surface detector. The cosmic ray events reconstructed from the data taken with the surface detector will be used in this thesis.

Auger has two ways of detecting cosmic ray showers which permit to derive properties (like energy, arrival time and direction) of the initial cosmic ray particle. The arrival time and direction will play important roles in my research.

The question which I will try to answer, is related to the origin of the high energy cosmic rays. Since some possible types of sources leave fingerprints in time, I will develop a method that makes use of the arrival times. The time characteristics of some objects are known from observations in the electro-magnetic spectrum. Adding this information about an object in the analysis creates the possibility to identify a source even though the angular resolution of the array is not sufficient to exclude other sources in the area.

Recently, there has been a lot of research on the topic of the origin of cosmic rays. This research has revealed a correlation of the highest energy cosmic rays with active galactic nuclei (AGN) [3]. This result shows how important it is to use all information available to identify the possible origins of the highest energy cosmic rays , as for now it is not known if AGN, or objects correlated with AGN are the sought after sources.

This thesis will consist of two parts. First, I will identify classes of objects that are possible cosmic ray accelerators which have a typical behavior in the time domain. Second, a method to analyze these sources is developed.

Chapter 2

Source Candidates

Traditional observations of the sky in the electro-magnetic spectrum learns us that a lot of objects show periodic fluctuations in their brightness. The underlying physics for the periodic fluctuations can be quite divers. Processes that one can think of are: stellar oscillations, binary interactions, eclipsing, rotation of irregularities at stellar surfaces, etc. Different processes lead often to different periodic brightness patterns. Different kinds of periodicity require different analysis methods. The method, that will be developed here, needs to be sensitive to small periodic signals. When dealing with statistics on small signals, one needs to know with a high precision what one is looking for, i.e. the objects under investigation will be systems with well known parameters. Another characteristic of the objects under investigation is their ability to accelerate particles up to extreme energies in order to produce high energy cosmic ray particles.

2.1 Pulsars

In 1967, the first pulsar has been detected by Jocelyn Bell and Antony Hewish [4] at the Mullard Radio Astronomy Observatory. After a few years of discussion, consensus was reached that the nature of the pulsating object is in fact a neutron star, an object already suggested as a possible outcome of stellar evolution by theorists some decades earlier [5]. Since then, 1776 pulsars have been detected in our galaxy. These neutron stars are believed to be objects that have a mass of $\approx 1.4\,\mathrm{M}_\odot$ and a radius of about 10 km. The pulsars have a beam in which photons are emitted in the radio domain of the electro-magnetic spectrum. This beam sweeps out in space and, when it hits the Earth, it appears as a peak in the radio intensity. The period of the radio pulses corresponds with the period of rotation. Pulsars have periods between 0.001 s and 10 s. These periods are known with very high precision. The uncertainty Δ_p in the period p is usually in the order of $\Delta_p \approx 10^{-10} \times p$. These well known periods make pulsars good objects to analyze, under the assumption that cosmic ray particles are emitted in the radio beam.
Another important property of pulsars is that they all show a slow down rate, i.e. $\dot{p} < 0$. This suggests that pulsars are loosing energy. Because the slow down rate $\dot{p}$ can be measured, the amount of energy lost can be calculated.

$$\frac{dE}{dt} = \frac{d}{dt}\left(\frac{1}{2} I\omega^2\right) = I\omega\dot{\omega} \tag{2.1}$$

In which ω is the angular velocity, and I the moment of inertia. Using the relation $p = 2\pi/\omega$ and assuming that the pulsar is a solid sphere with moment of inertia $I = \frac{2}{5}MR^2$ equation (2.1) becomes

$$\frac{dE}{dt} = \frac{2}{5}MR^2 \frac{2\pi}{p}\frac{d}{dt}\frac{2\pi}{p} = -\frac{8}{5}MR^2\frac{\pi^2}{p^3}\dot{p} \tag{2.2}$$

Using typical pulsar values, $M = 1.4\,\mathrm{M}_\odot$, R =10 km, p=0.4 s and $\dot{p} = 10^{-14.4}$, an energy loss of $\dot{E} = 1.7 \times 10^{45}\,\mathrm{eV\ s^{-1}}$ is obtained. It might be possible that a fraction of this energy loss is used in the acceleration of cosmic ray particles.
Additionally, the large magnetic field makes pulsars attractive cosmic ray candidates. Should an object accelerate a particle up to a certain energy E_{cr}, the particle should be confined to the source until it reaches this energy. The confinement of a charged particle depends on the spatial dimensions and the strength of the magnetic field of the source. The maximum energy a particle can obtain before escaping the system is given by [6]

$$E_{\mathrm{cr}} = 0.9ZBR \tag{2.3}$$

In which the energy is given in EeV (10^{18} eV), Z is the atomic number of the accelerated particle, B the magnetic field strength in μG in the accelerating region, and R the size of the source in kilo-parsec. For several sources this maximum energy is calculated as shown in the Hillas plot in Figure 2.1. The surface

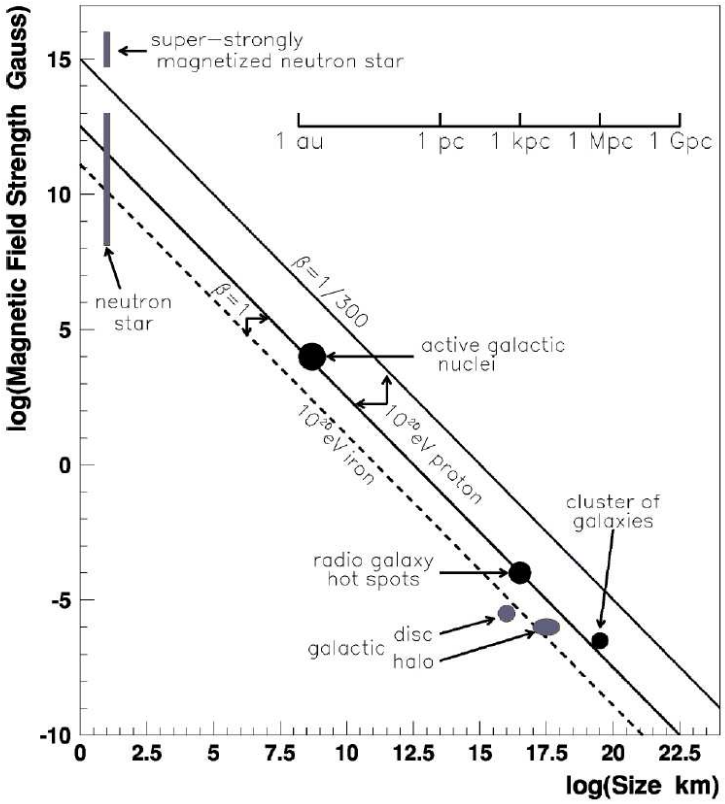

Figure 2.1: Astrophysical objects that are potentially able to accelerate the highest energetic cosmic ray particles.

magnetic field of a pulsar has a typical value of 10^{18} μG, and the size of a pulsar is roughly 10 km. If the particle in this case was a proton, its maximum energy would be $E_{\mathrm{cr}} = 2.9 \times 10^{20}$ eV.

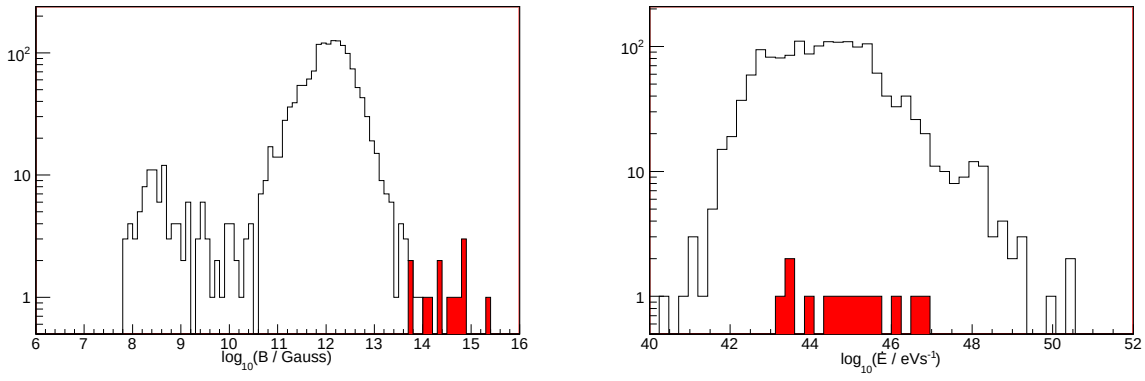

Figure 2.2: Left: Histogram of the magnetic field strength of the source candidates. White bars for the pulsars, red bars for the magnetars. Right: Histogram of the energy loss of the source candidates. White bars for the pulsars, red bars for the magnetars.

2.2 Magnetars

Another class of objects, similar to pulsars, are magnetars. Although pulsars already have extreme magnetic fields, magnetars are believed to have even stronger fields (Left Figure 2.2). These objects are possible outcomes of stellar evolution of extremely massive stars. These stars loose a lot of their mass (80%) in their supernova explosion. In this way, they are prevented from collapsing to a black hole. The remnant is a neutron star with a very high magnetic field.
There are two classes of objects that contain a magnetar: the Soft Gamma Repeaters (SGR's) and the Anomalous X-ray Pulsars (AXP). The SGR's show repetitive outbursts in gamma rays. This is different from Gamma Ray Bursts, that never come from the same location twice. The SGR are located near, or in the galactic plane, suggesting a galactic origin. In 1998, observations on the spin down of SGR 1900+14, with the Rossi X-Ray Timing Explorer, confirmed that the SGR's must be magnetars. The first anomalous X-ray pulsar has been detected in the seventies with the Uhuru X-ray space telescope. The nature of these objects have been under debate for decades, initially they were thought to be members of X-ray binaries. However, recent observations with INTEGRAL show that they are in fact magnetars.
When calculating the maximum energy a particle can obtain near these objects according to equation (2.3), using a magnetic field of $10^{21}\,\mu$G and a radius of 10 km, a maximum energy of $E_{\rm cr} = 2.9 \times 10^{23}\,$eV is obtained for protons.

Chapter 3

Tools & Tactics

3.1 Phase Diagrams

There are several types of periodicity and for each type there is an optimal way to analyze it. The periodicity that is considered in our research is a delta peaked periodicity. The assumption is that an astrophysical object produces at a particular phase of its period cosmic ray particles that hit our detector. This would result in fixed time intervals in the Arrival Time of the Cosmic Rays (ATCR's) corresponding with the period of the object. If the period of the object is known, a phase diagram can be made. A phase diagram is just a histogram of the phases for a known period. This histogram is filled with the ATCR *modulo* period p from the events that are selected around the object of interest. This can be regarded as the phase of the event with respect to the period of the (astrophysical) object. A significant flux would result in an excess of events at a particular phase, thus a peak in the phase diagram. The bin size of the phase diagram is defined by the uncertainties on the calculated phases. If the number of bins is large enough, the probability that the phase of a background event, which is not associated with the object, falls into one given bin will be small. Thus the number of background events per bin, can be described by a Poisson distribution.

$$P(i;\mu) = \frac{\mu^i e^{-\mu}}{i!} \tag{3.1}$$

$P(i;\mu)$ gives the probability of having i events in a bin. The mean μ is defined as N/B, with N the number of events in a phase diagram with B bins. The probability of having n or more events in one bin can be obtained from

$$P(\geq n) = \sum_{i=n}^{\infty} p(i) = 1 - P(< n) = 1 - \sum_{i=0}^{n-1} P(i) \tag{3.2}$$

From equation (3.2) the probability $Q(\geq n)$ of finding at least one bin with more than n background events in a phase diagram can be derived

$$Q(\geq n) = 1 - Q_0 = 1 - (1 - P(\geq n))^B \tag{3.3}$$

Q_0 is the probability of not having one bin with at least n events in the phase diagram. The Q value gives the Poissonian probability that the phase diagram contains at least one bin with n background events in it. So if Q is getting smaller, it becomes more unlikely that our phase diagram contains only background events. In what follows, the value of n is always chosen to be the maximum number of events in any bin in the phase diagram.

The Q value from equation (3.3) is an approximation that uses Poisson statistics. For low B and N this approximation will not be valid. For example, consider the case in which N=3 and B=2. What is the probability that this phase diagram contains at least one bin with two events in it? If you calculate $Q(\geq 2)$ with equation (3.3) then a value of Q =83.5 % is obtained. But this phase diagram must always have at least one bin with two or more events in it, therefore $Q = 1$. To make sure our analyses will not suffer from this effect, we compare the Q values from a simulation with the Q values of the Poisson statistics for typical parameters of our phase diagrams. In the simulation, 200 events are randomly distributed over B bins. This procedure is repeated 10^4 times, and for each phase diagram the probability that it contains one bin with n or more events in it is evaluated. In figure 3.1 this simulated value for Q is compared to Q obtained from equations (3.2) and (3.3) for $n = 2$ and $n = 5$, using the same parameters of the phase diagrams. If we take more than 100 bins, our approximation is valid within the statistical errors of the simulations.

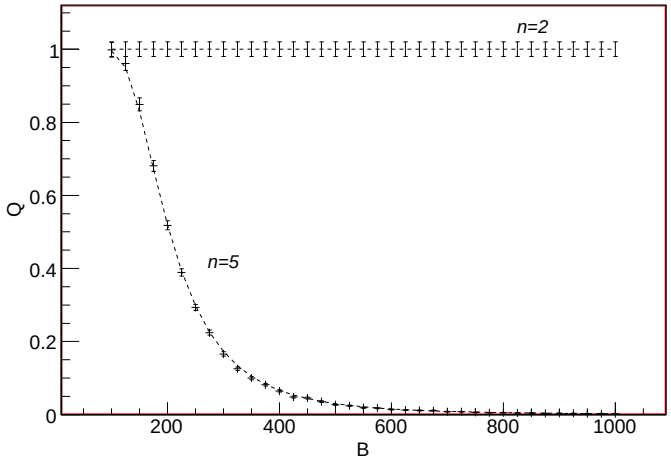

Figure 3.1: Comparison of the Q values obtained with Poisson statistics (dotted line) and the Q values from simulations (data points with error bars) for phase diagrams with 200 events in it.

Equation (3.3) gives us a relation between the number of bins B and the probability of having at least one bin with n events in it. In figure 3.2, the relation between Q and B is plotted for $n = 1...9$ and a

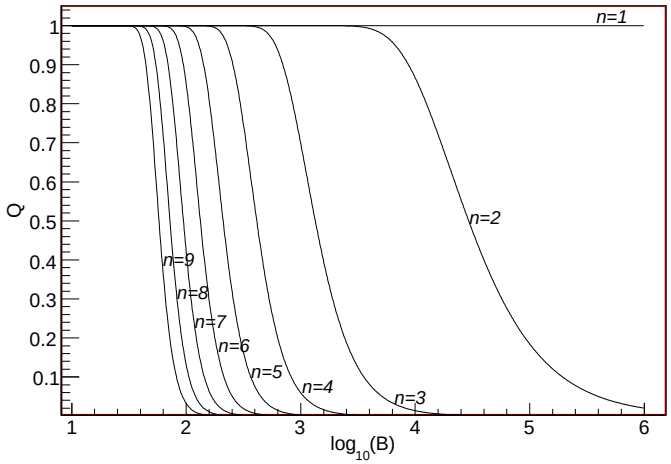

Figure 3.2: The probability Q of finding a bin containing at least n events for a phase diagram with B bins ($N = 200$ Poissonian distributed events). The lines present different values of n. The first line going down represents n=9 going further to the right n decreases.

phase diagram with N=200 events. The straight line at Q=1 corresponds to n=1. This means that the probability of finding a bin in the phase diagram with one event in it is 100%. That is perfectly reasonable because if $N \geq 1$ there is always one bin with at least one event in the phase diagram. When the requested number of events in a bin goes up, the number of bins needed to obtain a probability Q which is consistent with a background only hypothesis, decreases rapidly. The number of bins minimally needed to get Q below a certain value (Q=1 %,5 % or 10 %) for a given n is shown in figure 3.3. The number of bins required to reach below a certain value of Q is sharply increasing if the requested maximum number of events in one bin (n) is decreasing. The uncertainties on the phase are used to define B, thus for a low n these uncertainties should be small.
Another effect on the statistical outcome is the number of events N in each phase diagram. In figure 3.4 is this effect shown. The effect of increasing the number of background events N is that more bins B are needed to reach below a certain Q-value. This is what one would expect since N is defining the μ in equation (3.1). For low N one needs less bins B to obtain the same μ of the Poisson distribution. A lower μ results in a lower P (eq.(3.2)) for increasing n, thus also in a lower Q (eq.(3.3)). N is divided into two

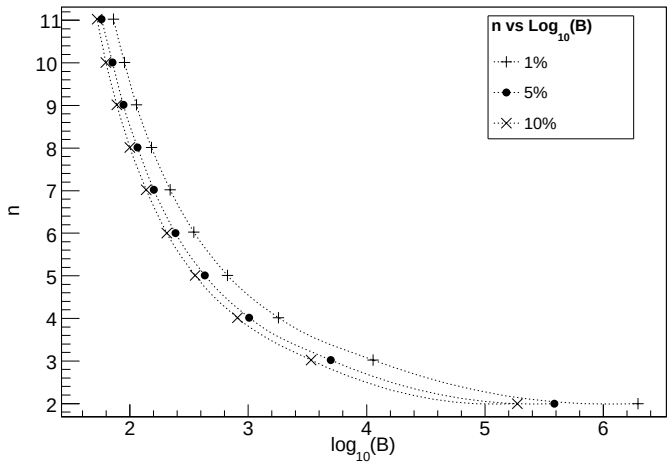

Figure 3.3: The number of bins B required to obtain a probability of Q=1%, 5% or 10% of finding a bin containing n or more events when generating $N = 200$ Poissonian distributed events.

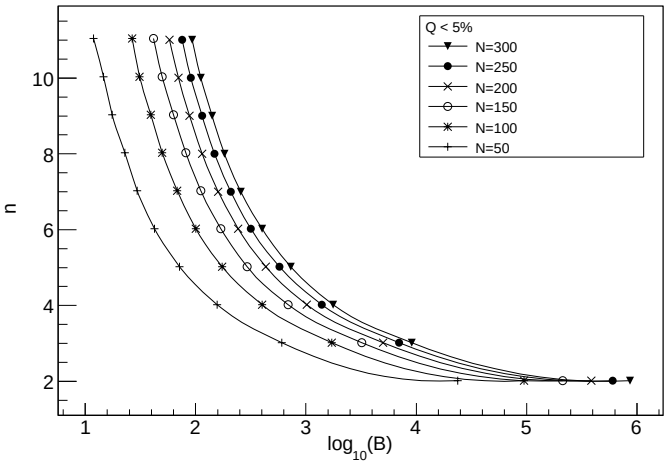

Figure 3.4: The number of bins B required to reach a Poissonian probability of Q <5% of finding a bin containing at least n events. Results for phase diagrams with $N = 50, 100, 150, 200, 250, 300$ Poissonian distributed events are shown.

parts, the events that fall in the bin with the maximum content n, and those that do not n_r. It is in fact the ratio n/n_r that defines Q. The larger this ratio, the smaller Q will be.

3.2 Search Strategy

The phase diagrams and their Q values are tools to analyze the data sets of events around the objects of our interest. However, the way they are produced does have some randomness in it. For example, the position of the bins in time are randomly chosen. Due to this effect, it might be possible that a significant signal is divided over two bins. In this case a possible source could not be noticed by just looking to the Q of its phase diagram. In order to avoid this effect, each phase diagram is produced ten times, and every time the bins are shifted by 10 % of the bin size.
There are more parameters of the phase diagrams that can be varied. For example, the number of events that are selected around an object of interest. Events are selected by defining an openings angle α with respect to the direction of the object. A logical value for α would be the uncertainty in the measured direction of the cosmic rays. However, in the Auger-observer definition of reconstructed events, no uncertainty in either right ascension or declination is given. To get a measurement of this uncertainty hybrid events are used. These events are recorded with both the fluorescence and surface detectors. Both

methods give the direction of cosmic rays. The difference between both reconstructed directions will be taken as the uncertainty on the direction of the events reconstructed with the surface detector. It is thus assumed that the uncertainty in the fluorescence measurement is smaller. In figure 3.5 this difference

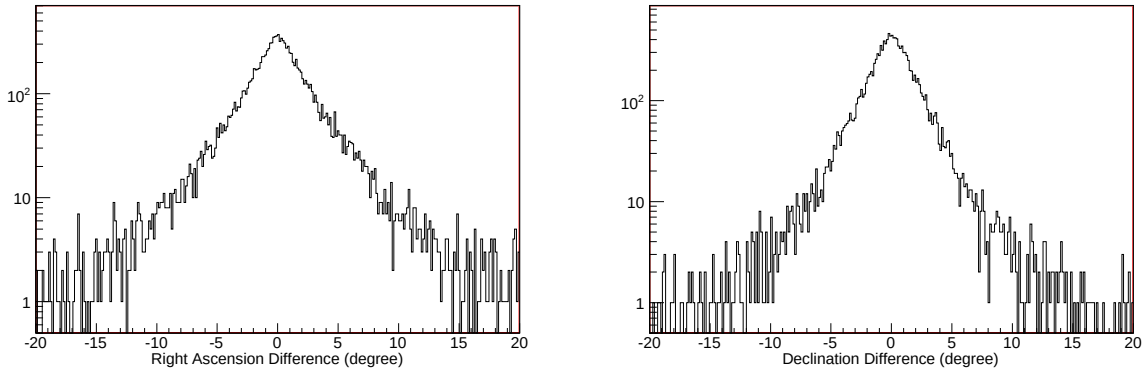

Figure 3.5: Difference in direction measurement by the fluorescence and surface detectors.

is shown and an uncertainty in the surface detector directional information of $\sim 2^\circ$ is adopted. Three different data sets with values of $\alpha = 1.5^\circ$, 2.0° and 2.5° are created. The value of 1.5° is used to increase the ratio between signal and background. The value of 2.5° is taken to reduce the probability that events from the object are left out.
Another option is to change the bin size. The way in which the minimum bin size is obtained is discussed in section 4.8. However, it is allowed to increase the bin size. In this case the method becomes more sensitive to less fixed periods. This takes into account that the calculated phase is not as well known as expected from section 4.8. In that section a dimensionless parameter κ is defined to make the bin size a little bit bigger. We decided to create phase diagrams with three different values of κ =1, ,1.5 and 2. One cannot go for a very large κ, because this means that the number of bins in the phase diagrams is reduced. Reducing the number of bins will influence the statistical probability, as discussed in section 3.1. For each object of interest the number of phase diagrams created will be $10 \times 3 \times 3 = 90$. Therefore, the value of Q can no longer be regarded as the statistical probability described in section 3.1, but rather as a quality factor of the peak. The strategy applied is to optimize the peak in the diagrams obtained with the surface detector data in the year 2006. Then we apply a cut on the Q-value. The phase diagrams that result in a Q-value <0.01 are selected as possible candidates for cosmic rays sources. For the selected candidates phase diagrams are created using the data from 2007 (until September) , using the settings that gave the minimal value of Q for the 2006 data. In these diagrams the same bin that gave the maximum in 2006 is being used to calculate the probability of containing at least the measured number of events. This probability is given by equation (3.2).

Chapter 4

Corrections, uncertainties and binning

4.1 Bary- and geocentric corrections

As some Polish dude proved that the Earth is not the center of the universe but just some rock rotating around the Sun [7], we have to make additional corrections in the ATCR's. The rotation of the Earth around the sun creates a path length difference for cosmic ray particles coming from the same source. The difference in arrival time can go up to 16 min. But if the direction of the source and the position of the Earth are known it is possible to correct for this effect. Actually, the Earth is not rotating around the Sun but around the barycenter of the solar system. This barycenter is just outside the Sun's surface. If the Pierre Auger Detector was placed at the barycenter of the solar system the path length between the object and the detector would be constant. A time correction on the arrival times of the events will be preformed, this virtually moves the Pierre Auger site to the barycenter of the solar system.

The correction is made using routines from the positional astronomy library SLALIB/C[8]. The most ac-

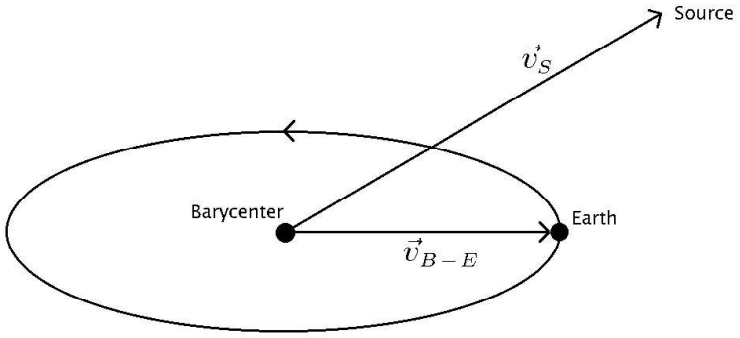

Figure 4.1: The barycentric correction is made by taking the inner product of $\vec{v}_{B-E}$, the vector that gives the position of the decenter in the Barycentric Celestial Reference System, and $\vec{v}_S$, the positional vector in the that points to the source (also given in the BCRS).

curate way to do so uses the function *epv.c*, which calculates the Earth's geocentric position and velocity with respect to the Barycentric Celestial Reference System(BCRS). The axes in the BCRS are defined in the same way as the equatorial equinox system (normal right ascension (RA) and declination (Dec)) with the origin in the barycenter. The *epv.c* routine returns a Cartesian vector $\vec{v}_{B-E}$ with a length equal to the distance from the barycenter to the Earth expressed in Astronomical Units (1 AU=149598000 km) in the BCRS. The directional vector to the source $\hat{\Omega}_S$ can be transformed from a spherical coordinate system to a unit vector $\vec{v}_S$ in a Cartesian coordinate system. This is straightforward $\hat{x} = \cos(RA)\cos(Dec)$, $\hat{y} = \sin(RA)\cos(Dec)$ and $\hat{z} = \sin(Dec)$. Taking the inner product of $\vec{v}_{B-E}$ and $\vec{v}_S$ gives the path length difference traveled by CR's going to Earth or to the barycenter of our solar system. The uncertainty in this correction is maximally 13.4 km, which corresponds with an uncertainty in the time correction of $\sim 43\,\mu$s. However, to reach this precision another correction still has to be performed. As the Pierre Auger observatory is not located at the center of the Earth, a time correction to the center of the Earth has to be made. The error on the ATCR's due to the rotation of the Earth around its own axis is maximally $R_\oplus/c \approx$

0.021 s (note that the maximum path length difference is not $2R_\oplus$, because if the observatory is on the opposite side of the Earth with respect to the direction of the object of interest, no cosmic rays from that direction will be detected). This error due to the rotation of the Earth seems small, but it turned out to be a significant factor in the selection of pulsars. Without correcting for the Earth's rotation only five pulsars would survive the selection criteria for the analysis instead of the 65 pulsars selected in this research (section 6.1.1). So in order to reduce the errors due to the motion of the Earth, a transformation needs to be made in such a way that the Pierre Auger observatory appears to be in its center. Therefore, the distance from the center of the Earth to the observatory needs to be known. First of all the Earth is not exactly a perfect sphere but slightly flattened due to the Earth's rotation. The radius of the Earth $R_\oplus$ at a given latitude θ is given by the following equation,

$$R_\oplus = R_\oplus(\theta) = \sqrt{\frac{(a^2\cos(\theta))^2 + (b^2\sin(\theta))^2}{(a\cos(\theta))^2 + (b\sin(\theta))^2}} \tag{4.1}$$

With a the equatorial radius and b the polar radius. The value of a is 6378.135 km, the value of b is 6356.750 km and the latitude θ of the Pierre Auger Observatory is -35°. Using equation(4.1), one obtains an $R_\oplus(\theta)$ of 6371.139 km. This is the radius of the Earth at sea level, but the Pierre Auger observatory is at an altitude h of 1400 m above sea level. So the distance r to the center of the Earth will be $r = R_\oplus(\theta)+h=$ 6772.539 km. To calculate the difference in path length by a signal from direction $\hat{\Omega}_s=(RA, Dec)$ between the center of the Earth and our observatory, the position of the observatory needs to be known at the time of detection of the signal. Taking the inner product of the vector $\vec{r}_{obs}$, that gives the position of the observatory, and the direction of the signal $\hat{\Omega}_s$, the difference in path length Δl traveled by the signal is obtained.

$$\Delta l = \hat{\Omega}_s \cdot \vec{r}_{obs} \tag{4.2}$$

It is possible to calculate the vector $\vec{r}_{obs}$ in the (RA, Dec) system, which corresponds to sitting in the center of the Earth and finding the declination and right ascension of our detector. Of course sitting in the center of the Earth looking trough thousands of kilometers of rocks and dirt is not really an option, but this can be calculated. The declination of our observatory is fixed and corresponds to the latitude of observatory, $Dec = Latt$. The right ascension is a little bit more complicated because it varies with time. The RA of the observatory corresponds with the well known *local sidereal time* (LST). The LST is calculated using the timestamp created when recording the event.

The timestamp of an event is expressed in GPS time. This time frame is 19 sec behind the widely used

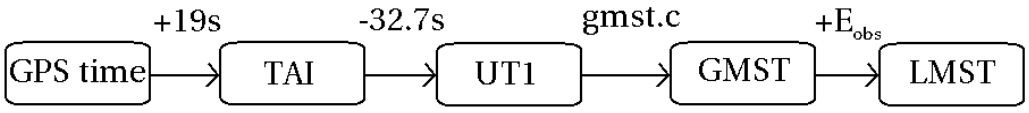

Figure 4.2: The steps to go from a GPS time to the local mean sidereal time.

International Atomic Time (TAI). This time is measured with the input of many atomic clocks around the world, and is regarded as the primary time standard. Furthermore, it is used for the definition of the *SI* second. However, we are not interested in the decay of atoms but in positions on the sky. Thus we need a time based on the rotation of the Earth. This rotation is not constant in time. The standard clock based on the rotation of the Earth is the *Universal Time* (UT1), which is based upon the observed rotation of the Earth with respect to the sun. There is a difference between the TAI and the UT1. This difference is measured by the *International Earth Rotation Service* (IERS), thus one can correct for this difference. The measured difference between UT1 and TAI in 2006 was UT1-TAI=-32.7 s [1]. The UT1 gives the rotation of the Earth with respect to the sun, but the rotation of the Earth with respect to the stars (or other distant objects) is needed. The UT1 must be transformed to a timescale that is based on the rotation of the Earth with respect to distant sources. The standard for this timescale is the *Greenwich Mean Sidereal Time*. The function *gmst.c* from the SLALIB [8] provides this functionality. This function takes the UT1 and returns the sidereal time at the zero meridian. The Greenwich sidereal time must be converted to the *local mean sidereal time* at the Pierre Auger observatory. This is done by adding the eastern longitude of the observatory E_{obs}.

$$LMST = GMST + E_{obs} \tag{4.3}$$

[1] http://hpiers.obspm.fr/eop-pc

The LMST can be expressed as an angle, which gives right ascension of the observatory at a given time. Let θ_{obs} be the declination of the observatory, ϕ_{obs} the right ascension of the observatory, θ_s the declination of source, ϕ_s the right ascension of the source and r the distance of the observatory with respect to the center of the Earth. Then equation (4.2) becomes

$$\Delta l = \hat{\Omega}_s \cdot \vec{r}_{obs} = r\Big[\cos(\theta_{obs})\cos(\theta_s)\big[\cos(\phi_{obs})\cos(\phi_s) + \sin(\phi_{obs})\sin(\phi_s)\big] + \sin(\theta_{obs})\sin(\theta_s)\Big] \tag{4.4}$$

Assuming that the signal travels with the speed of light c, then the following time correction Δt_E has to be applied on the arrival time of the signal.

$$\Delta t_E = \frac{\Delta l}{c} \tag{4.5}$$

After preforming this correction the uncertainty on the ATCR's is the uncertainty on the barycentric correction, $\sim 43\,\mu$s.
To check the time corrections, two plots are created and shown in figure 4.3. From the left plot in figure

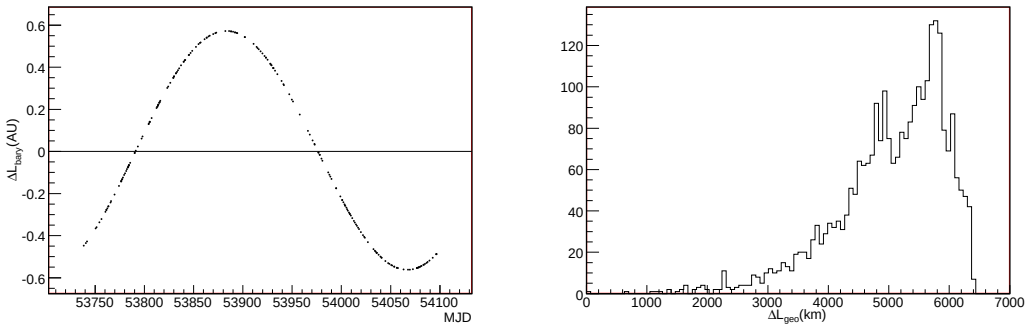

Figure 4.3: The time corrections. Left: The barycentric correction for a data set taken with an openings angle of two degrees around a source. Right: The geocentric correction for data around several sources.

4.3, we can see that the time corrections for the barycenter are periodic with a period of one year. This is what one would expect. From the right plot in figure 4.3, we see the corrections in path length for the geocentric correction. Also here there is no conflict with the corrections and what one would expect. All values are between 0 and 6772.539 km with most of the events between 4000 km and 6772.539 km. This just means that the detector is more sensitive to cosmic rays that are orthogonal to the plane of the surface of the detector than to cosmic rays that arrive from a more horizontal direction.

4.2 Velocity corrections

If the cosmic ray particles are massive particles, there will be a difference between their arrival times and the arrival time of light from the same source. This difference depends on the energy of the particle, and can be calculated as follows. If L is the distance that particles have to travel, and u the velocity of the massive particle, the time difference ΔT is given by

$$\Delta T = \frac{L}{u} - \frac{L}{c} = \frac{L}{\beta c} - \frac{L}{c} = \frac{L}{c}\Big(\frac{1}{\sqrt{1-\gamma^{-2}}} - 1\Big) \simeq \frac{L}{2c\gamma^2} \tag{4.6}$$

With $\beta = u/c$ and γ the Lorentz factor $1/\sqrt{1-\beta^2}$. For a neutron, with an energy of $E = 10^{18}$ eV, which travels $3.0{\times}10^4$ ly through space, the time difference with respect to a photon emitted at the same source at the same time is $\Delta T \simeq 4.7 \times 10^{-7}$ s. For a neutron with an energy of $E = 10^{17}$ eV the time difference is about $\Delta T \simeq 4.7 \times 10^{-5}$ s and becomes more significant. However, as is shown in section 5.2, the only massive particles taken into consideration are neutrons, and for these particles an energy cut will be applied at $\sim 3 \times 10^{18}$ eV. For these energies the time difference between light and a neutron becomes negligible.

4.3 Pulse Width

The assumption is made that the cosmic ray particles from our candidate sources are emitted in the same pulse as the electro-magnetic radiation. The geometry of the pulse can be characterized by the pulse

width w_{50}, which is the width of the pulse at 50 % of the pulse peak. The value of w_{50} will be the estimate for the width of the cosmic ray beam.

4.4 Intermezzo

After completing my analysis I found an article from the MAGIC γ-ray telescope [12] in which the phase calculation was different from mine. In my analysis the time derivatives of the rotational frequency of the pulsars was neglected when calculating the phases. However, it turned out that the time derivatives of the frequency need to be taken into account to obtain the required precision, so I had to redo the analysis. However, including the first and second time derivatives puts additional constraints on the number of pulsars that can be used (17 instead of 65). The result of reducing the number of useful pulsars is that none of the pulsars passed the selection criteria after the peak optimization (Section 5.4). In the *initial* analysis there were several pulsars that did pass the selection criteria, and could be analyzed further. In order to show how to continue after selecting a pulsar as a source candidate, we decided to also show the results of the *initial* analysis. In the parts were the initial phase calculation is used, it will be mentioned in the title of the sections. The sections based on the correct phase calculation will be indicated with *final* in the titles.

4.5 *Initial* Phase Calculation

After applying the bary- and geocentric corrections, the phase t_{phase} of the ATCR with respect to the pulsar period p can be calculated as:

$$t_{\text{phase}} = t - \text{floor}\big(t/p\big) \times p \tag{4.7}$$

Where the function floor rounds down its argument to an integer, and t =ATCR$-t_0$ is the time passed since the beginning t_0 of the dataset from which events are selected. The maximum uncertainty δ_p on the phase due to the uncertainty Δ_p on the pulsar period is given by

$$\delta_p = \text{floor}\big(T/p\big) \times \Delta_p \tag{4.8}$$

With T the time interval in which the data is taken.

4.6 *Final* Phase Calculation

After applying the bary- and geocentric corrections on the ATCR, the phase ϕ_j with respect to the pulsar can be calculated. This can be done by counting the number of rotations N_{j} from time t_0. Let t_j be the arrival time of a cosmic ray, then N_{j} is given by

$$N_{\text{j}} = \int_0^{t_{\text{j}}-t_0} f(t)dt \tag{4.9}$$

With $f(t)$ the rotation frequency at time t, which can be approximated by

$$f(t) \approx f_0 + \dot{f}_0 t + \frac{1}{2}\ddot{f}_0 t^2 \tag{4.10}$$

Were f_0, $\dot{f}_0$, and $\ddot{f}_0$ are the rotation frequency, its first, and second time derivative at time t_0 respectively. These values can be obtained from the ATNF catalogue were the rotational frequencies, and their time derivatives, are given for a certain epoch (t_0). Equation (4.9) then becomes:

$$N_{\text{j}} = \int_0^{t_{\text{j}}-t_0} (f_0 + \dot{f}_0 t + \frac{1}{2}\ddot{f}_0 t^2)dt = f_0(t_{\text{j}} - t_0) + \frac{1}{2}\dot{f}_0(t_{\text{j}} - t_0)^2 + \frac{1}{6}\ddot{f}_0(t_{\text{j}} - t_0)^3 \tag{4.11}$$

Taking the decimal part of N_{j} gives the corresponding phase ϕ_{j} of the pulsar for a cosmic ray with arrival time t_j. The phases ϕ_{j} are used to fill the phase diagrams described in section 3.1. The uncertainty on the calculated phase depends on the uncertainties on f_0, $\dot{f}_0$ and $\ddot{f}_0$.

$$\Delta\phi = \sqrt{\Big(\Delta f_0(t_j - t_0)\Big)^2 + \Big(\frac{1}{2}\Delta\dot{f}_0(t_j - t_0)^2\Big)^2 + \Big(\frac{1}{6}\Delta\ddot{f}_0(t_j - t_0)^3\Big)^2} \tag{4.12}$$

However, this gives the uncertainty on the phase if it was calculated from epoch time t_0, and we want to know the uncertainty over the period of our measurements. The data for this analysis is taken between January 2006 (t_1) and December 2007 (t_2). With equation (4.10) the rotational frequency on t_1 becomes

$$f_1 = f(t_1) \approx f_0 + \dot{f}_0(t_1 - t_0) + \frac{1}{2}\ddot{f}_0(t_1 - t_0)^2 \tag{4.13}$$

and the uncertainty on the frequency f_1 becomes

$$\Delta f_1 = \sqrt{\left(\Delta f_0\right)^2 + \left(\Delta \dot{f}_0(t_1 - t_0)\right)^2 + \left(\frac{1}{2}\Delta \ddot{f}_0(t_1 - t_0)^2\right)^2} \tag{4.14}$$

A similar approximation can be made for the first time derivative of the frequency

$$\dot{f}_1 = \dot{f}(t_1) \approx \dot{f}_0 + \ddot{f}_0(t_1 - t_0) \tag{4.15}$$

And the uncertainty on this becomes

$$\Delta \dot{f}_1 = \sqrt{\left(\Delta \dot{f}_0\right)^2 + \left(\Delta \ddot{f}_0(t_1 - t_0)\right)^2} \tag{4.16}$$

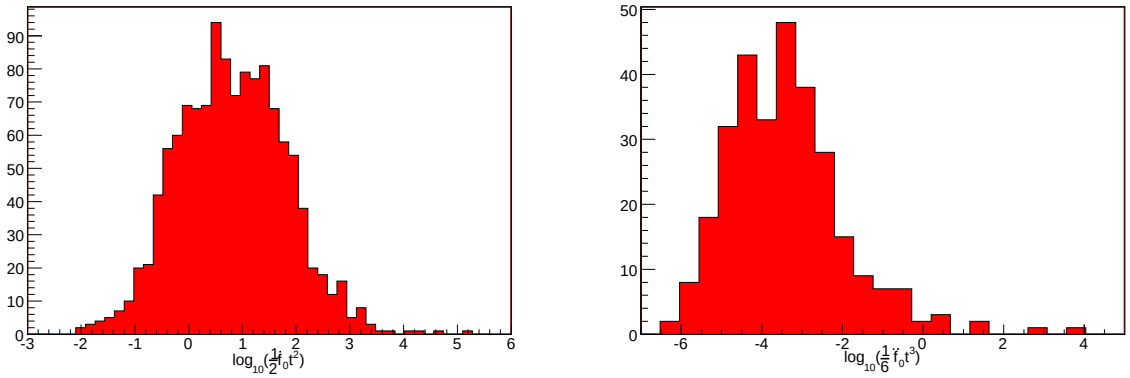

Figure 4.4: Contribution for the calculation of the phase from the $\dot{f}_0$(left) and the $\ddot{f}_0$ if t= 2 years.

For the second order time derivative we assume that it stays constant over time, $\ddot{f}_0 = \ddot{f}(t) = \ddot{f}_1$. Also the uncertainty on this is assumed to be constant $\Delta\ddot{f}_0 = \Delta\ddot{f}(t) = \Delta\ddot{f}_1$. The number of rotations of the pulsar at time t_j after time t_1 is given by

$$N_\mathrm{j} = f_1(t_\mathrm{j} - t_1) + \frac{1}{2}\dot{f}_1(t_\mathrm{j} - t_1)^2 + \frac{1}{6}\ddot{f}_1(t_\mathrm{j} - t_1)^3 \tag{4.17}$$

And the maximum uncertainty on N_j, and hence on the calculated phase ϕ_j, becomes

$$\Delta N = \Delta\phi = \sqrt{\left(\Delta f_1(t_2 - t_1)\right)^2 + \left(\frac{1}{2}\Delta \dot{f}_1(t_2 - t_1)^2\right)^2 + \left(\frac{1}{6}\Delta \ddot{f}_1(t_2 - t_1)^3\right)^2} \tag{4.18}$$

4.7 *Initial* Binning

The size of the bins in the phase diagrams should always be bigger than the uncertainty δ_ph on the calculated phase. This uncertainty δ_ph will be used to define the bin size b, and hence the number of bins B. The uncertainty δ_ph is calculated from several, independent, contributions given in the previous sections.

$$\delta_\mathrm{ph} = \sqrt{\delta_\mathrm{cor}^2 + \delta_\mathrm{GPS}^2 + \delta_p^2 + w_{50}^2} \tag{4.19}$$

δ_cor is the uncertainty discussed in section 4.1 and is maximally 43 μs, δ_GPS is the uncertainty on the timestamps of the surface detector and is smaller than $\sim$10 μs, and δ_p is defined by equation (4.8). ¿From equation (4.23) the minimum bin size can be defined as:

$$b_\mathrm{min} \equiv \delta_\mathrm{ph} \tag{4.20}$$

Introducing a dimensionless parameter $\kappa \geq 1$, the bin size b can be varied

$$b = \kappa b_{\min} \tag{4.21}$$

The numbers of bins B for a phase diagram with period p will be given by

$$B = \frac{p}{b} \tag{4.22}$$

¿From equation (4.19) and (4.22) it can be concluded that the phase diagrams with most bins are those with relative slow periods($p > 0.3\,\mathrm{s}$) and small pulse widths.

4.8 *Final* Binning

The size of the bins in the phase diagrams should always be bigger than the uncertainty δ_{ph} on the phase. This uncertainty δ_{ph} will be used to define the bin size b, and hence the number of bins B. The uncertainty δ_{ph} is calculated from several, independent, contributions given in the previous sections. For a pulsar with a period p this becomes

$$\delta_{\mathrm{ph}} = \sqrt{\left(\frac{\delta_{\mathrm{cor}}}{p}\right)^2 + \left(\frac{\delta_{\mathrm{GPS}}}{p}\right)^2 + \left(\Delta\phi\right)^2 + \left(\frac{w_{50}}{p}\right)^2} \tag{4.23}$$

δ_{cor} is the uncertainty discussed in section 4.1 and is maximally $43\,\mu\mathrm{s}$, δ_{GPS} is the uncertainty on the timestamps of the surface detector and is smaller than $\sim 10\,\mu\mathrm{s}$, and $\Delta\phi$ is defined by equation (4.18). ¿From equation (4.23) the minimum bin size can be defined

$$b_{\min} \equiv \delta_{\mathrm{ph}} \tag{4.24}$$

Introducing a dimensionless parameter $\kappa \geq 1$, the bin size b can be varied

$$b = \kappa b_{\min} \tag{4.25}$$

The numbers of bins B for a phase diagram will be given by

$$B = \frac{1}{b} \tag{4.26}$$

Chapter 5

Constraints

5.1 Galactic magnetic field

Electrically charged particles passing through the milky way are bent in the galactic magnetic field. Much is still unknown about the structure and the strength of this field [9]. Current estimates on the strength of the large scale magnetic fields are in the order of $\sim \mu$G. The radius of curvature R_{curv} of a charged particle moving through a magnetic field is given by equation (5.1). This radius is a measure for the distance-scale at which directionality is lost. Suppose we have a proton with mass m_{p} and an energy of 10^{18} eV. This results in a Lorentz factor γ of 10^9. Then R_{curv} is given by

$$R_{\text{curv}} = \frac{p}{qB} = \frac{\gamma m_{\text{p}} v}{qB} \approx \frac{\gamma m_{\text{p}} c}{qB} = 3.3 \times 10^3 \,\text{ly} \tag{5.1}$$

With p the momentum of the particle, q the charge of the particle, and B the magnetic field of the galaxy. If $R_{\text{curv}} >> R_{\text{G}}$ with R_{G} the (scale) radius of the galaxy, the direction measured at Earth contains information on the direction of the origin of the proton. However, the distance from the Sun to the center of our galaxy is $\approx 2.6 \times 10^4$ ly, which is an order of magnitude higher than R_{curv}. Charged protons (or nuclei) with energies of 10^{18} eV that travel on galactic scales loose their directional information. Since events are selected using the direction of the object it is crucial that the selected cosmic rays contain directional information. Therefore, the analysis will only be sensitive to neutral particles. However, there is no way to actually select neutral particles in our data set. The above means that should we see a signal, neutral particles of extreme energies are emitted from the source.

5.2 Lifetime of the neutron

One of the possible cosmic ray candidates for which the method is sensitive is the neutron. However, the neutron has a decay time of τ=900 s, thus the question becomes whether the neutron travels fast enough to arrive at Earth before decaying. In our frame of reference the decay time τ' if given by

$$\tau' = \gamma\tau \tag{5.2}$$

A neutron has a decay length of 2.85×10^{-5} ly, thus when it needs to travel a distance of $3{\times}10^4$ ly, a γ-factor of 10^9 is required. As a neutron has a mass of 939.573 MeV c^{-2}, its required energy becomes:

$$E = mc^2 = \gamma m_0 c^2 = 1.0 \,\text{EeV} \tag{5.3}$$

In order for the method to be sensitive for neutrons, an energy cutoff E >1 EeV should be applied. However, the lifetime is defined as the time in which $1 - 1/e \approx 63\,\%$ of the particles decay. In the following neutron-analysis, only events with energies above $E = 3 \times 10^{18}$ eV are considered. In that case the γ-factor of the neutrons will be $\gamma = 3.2 \times 10^9$. The result is that 72 % of the selected neutrons emmited at a distance of $3{\times}10^4$ ly arrive at Earth.

5.3 Photon sensitivity of the surface detector

Other possible candidate-particles for this research are photons. However, photon interactions with the atmosphere differ substantially from interactions between protons, neutrons or nuclei and the atmosphere.

The number and nature of the particles at ground level is substantially different if the primary particle is a proton. Due to this effect the sensitivity of the surface detector for photons is still unknown. It is possible to search for a possible photon-signal, even at energies below 10^{18} eV, but it is not yet possible to convert this measurement into a flux (limit).

5.4 Analysis

In our analysis the directional information and timestamps of the recorded cosmic rays are used. We test whether these two properties correspond to similar properties of known astrophysical objects that give periodic pulses in the electro-magnetic spectrum. From the arrival times of cosmic rays, originating out of the direction of these objects, it is calculated if there is a correlation with the pulse periods. These tests make use of the assumption that the cosmic ray particles are emitted in the same cone (with the same openings angle) as the electro-magnetic radiation.
As concluded in section 5.1, we will only test if there are high energy neutral particles emitted. Therefore, a correlation can only be found if the cosmic ray particles are neutrons or photons.
The analysis is performed twice, once for all recorded events and once for events with energies above 3 EeV and a zenith angle cut of $\theta < 60°$. This data cut corresponds to the energy at which the detector becomes fully sensitive. The zenith angle cut is determined by the reconstruction. Below 60° the uncertainties on the reconstructed parameters are well understood. Another advantage of the energy-cut is that above this minimum energy, the majority of cosmic ray neutrons would not decay before reaching Earth (section 5.2).
From the peak optimization, described in section 3.2, candidate sources are selected. In a second, independent, dataset, it is calculated if there is a significant *signal*. This means that a phase diagram with the optimized settings will be constructed for this second dataset. The bin that gave the peak in the first dataset is then considered in the second set. The unified approach is taken to establish if this bin is in agreement with background, or if a signal is required at the 95 % confidence level (ref. [16]). The number of background events is calculated from the average number of events per bin.
In order to calculate the flux (limit) from the measurement, the sensitivity of the detector needs to be known. As discussed before, this is not the case for low energy photons. For the dataset with events above 3 EeV the signal could exist out of neutrons, thus in this case a limit on an assumed neutron flux will be derived.
The data used are the surface detector data from the Auger Observer. Two independent data sets are taken, the 2006 data, and the data recorded between January 1st 2007 and September 9th 2007. The data from 2006 is used to optimize a possible signal, as described in section 3.2. The peak optimization result in candidates sources. The 2007 data is used to verify if these candidates are present in an independent data set.
The objects that are under investigation are pulsars and magnetars. The parameters of the pulsar are taken from the ATNF pulsar catalogue. For the parameters of the magnetars the SGR/AXP Online Catalog [1] is used.

[1] http://www.physics.mcgill.ca/ pulsar/magnetar/main.html

Chapter 6

Pulsars

6.1 *Initial* Analysis

6.1.1 Pulsar Selection

A selection is made from the pulsars listed in the ATNF pulsar catalogue. Using the pulsar parameters obtained from this catalogue, and equation (4.22), the maximum number of bins can be calculated. A pulsar is selected when the resulting phase diagram contains more than 100 bins. From this selection, the pulsars in binaries systems are excluded. Therefore, corrections on the arrival time due to binary orbits are not needed. In figure 6.1 the pulsar population, excluding binaries, is given in galactic coordinates.

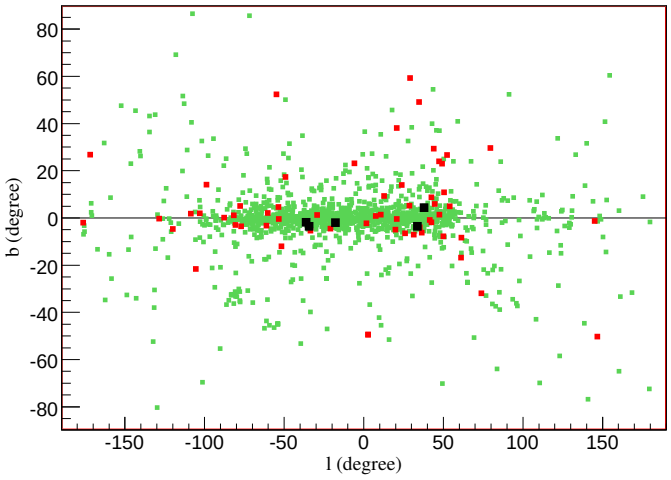

Figure 6.1: The pulsar population of all, non binary, pulsars is given in green squares. The selection of pulsars that are suitable for our method are given by the red squares. The five black squares are the candidate pulsars selected after peak optimization.

From the total of 1776 pulsars, 65 pulsars remain after applying the selection criterion (red squares). This corresponds to $\sim 3.7\,\%$ of the total pulsar population. The periods of the selected pulsars are between 0.3 s and 10 s. The search strategy, described in section 3.2, is applied on the selected pulsars. This results in five candidates sources, the black squares in figure 6.1.

6.1.2 Candidates

After performing the peak optimization procedure described in section 3.2, phase diagrams from five pulsars gave a Q value below 0.01. The settings of the corresponding phase diagrams are given in table 6.1.2. The bin offset is expressed in a fraction of the bin size. For several phase diagrams the minimum value of Q was constant over a range of bin offsets. In that case, the middle of such a range was chosen. Pulsar PSR J1703-4442 is present twice in the dataset, both with and without an energy cut. The optimized settings for both cases are different.

Pulsar	Q	α	κ	Offset
PSR J1538-5750	0.007	2.5°	2	0
PSR J1905-0056	0.008	1.5°	1	0.1
PSR J1158-5756	0.007	1.5°	1	0.55
PSR J1845-0623	0.006	2.0°	2	0.4
PSR J1703-4442	0.008	2.5°	2	0.1
PSR J1703-4442	0.002	1.5°	1.5	0

Table 6.1: The candidate pulsars and the setting for the phase diagrams that resulted in a Q<0.01. The first five pulsars are selected from the total surface detector data of 2006. The last pulsar is selected from 2006 data, applying an energy (E >3 EeV) and zenith angle ($\theta < 60°$) cut.

The dataset of 2007 is used to search for events around these five pulsars, using the openings angle α listed in table 6.1.2. For these events phase diagrams are created according to the parameters given in table 6.1.2. The phase diagrams that resulted in the minimum Q values in 2006, and their corresponding phase diagrams using the 2007 data are shown in figures 6.2, 6.3, 6.4, 6.5, 6.6 and 6.7.

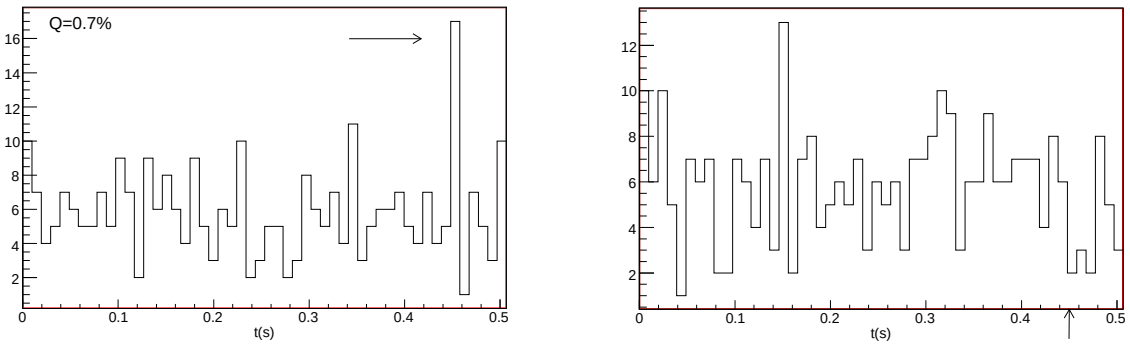

Figure 6.2: The phase diagrams for 2006 (left) and 2007 (right) for PSR J1538-5750.

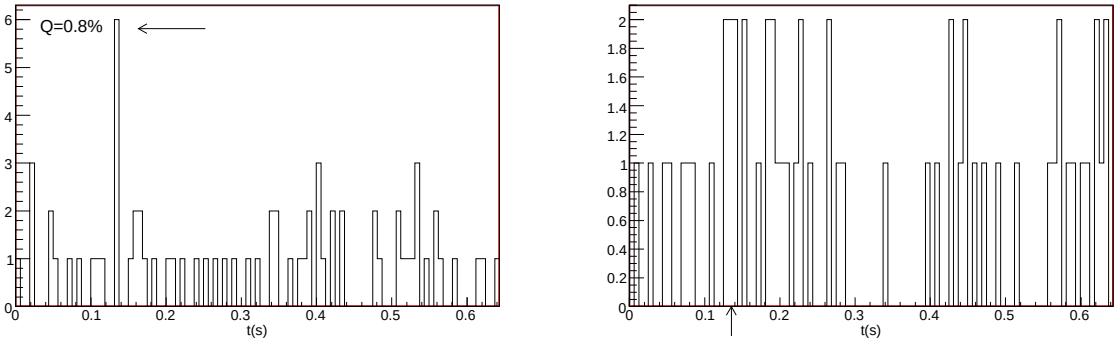

Figure 6.3: The phase diagrams for 2006 (left) and 2007 (right) for PSR J1905-0056.

The arrow in each of the 2006 phase diagrams is pointing to the maximum value. The arrows in the 2007 phase diagrams are pointing to the 2006 "signal"-bin. Using equation (3.2), the Poisson probability $P(\geq n)$ of measuring at least n events in this bin is calculated. The parameters and the results of this calculation are given in table 6.1.2. As seen from table 6.1.2 all results are in agreement with a background hypothesis. This means that no *signal* is significant with respect to the background. Therefore, a 95 % upper limit n_s on the signal will be derived.
To derive n_s, the *unified approach to the classical statistics analysis of small signals* by Feldman and Cousins [16] is used. As an estimate of the background, the mean bin content μ is taken. The 95 % upper bounds of the confidence belt are given in table 6.1.2. In those cases where no energy cut was placed on the data, a photon hypothesis is tested, and no flux limit can (yet) be derived, as discussed in section 5.4. In the remaining case where a 3 EeV cut is applied to the data, a neutron hypothesis is tested, and a flux

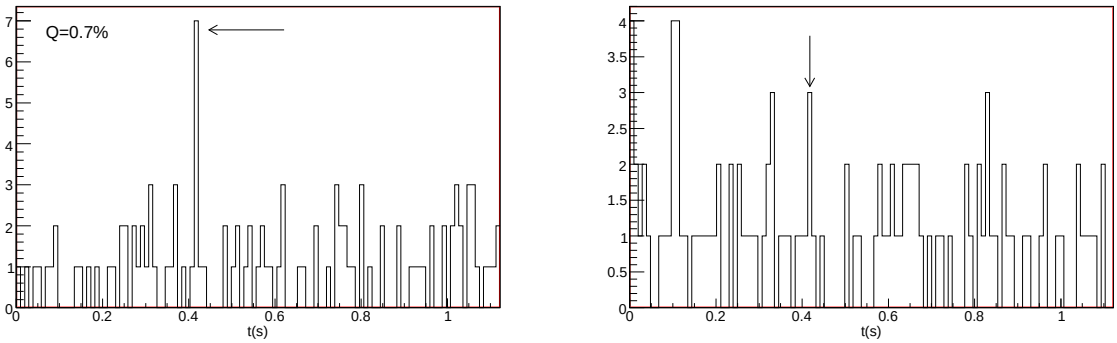

Figure 6.4: The phase diagrams for 2006 (left) and 2007 (right) forPSR J1158-5756 .

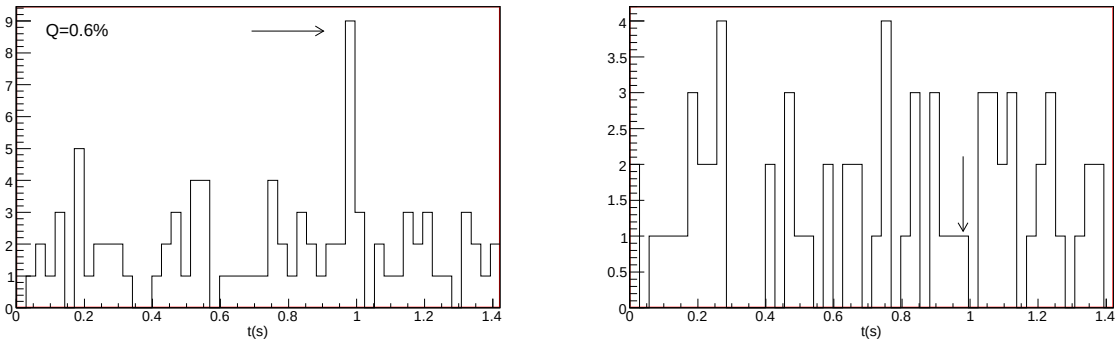

Figure 6.5: The phase diagrams for 2006 (left) and 2007 (right) for PSR J1845-0623.

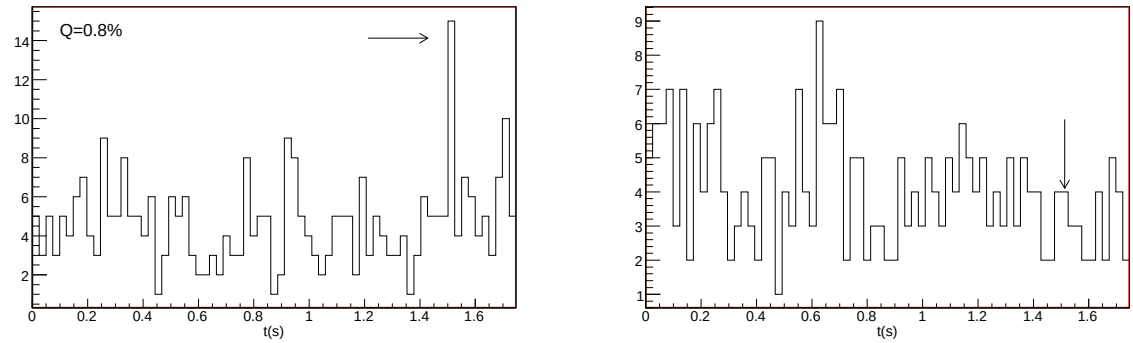

Figure 6.6: The phase diagrams for 2006 (left) and 2007 (right) for PSR J1703-4442.

Pulsar	n	μ	$P(\geq n)$
PSR J1538-5750	2	5.81	98 %
PSR J1905-0056	2	0.55	11 %
PSR J1158-5756	3	0.96	7.3 %
PSR J1845-0623	4	1.36	74 %
PSR J1703-4442	1	4.04	57 %
PSR J1703-4442	0	0.042	100 %

Table 6.2: The number events n (2007) in the 2006 "signal"-bin. μ is the mean number of events per bin. $P(\geq n)$ is the probability of measuring at least n events in a bin, assuming a background hypothesis. The first five pulsars are from the dataset with no cut. The last listing is from the dataset with energy and zenith angle cuts.

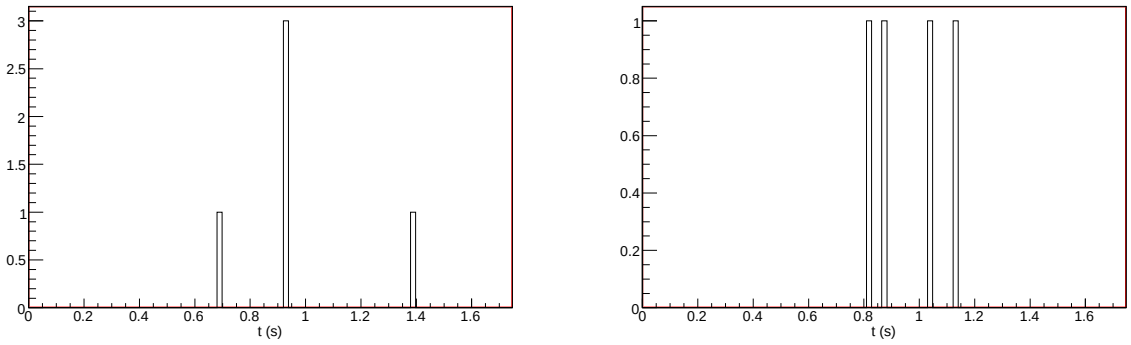

Figure 6.7: The phase diagrams for PSR J1703-4442 with the data cut. Left: The phase diagram with a $Q = 0.2\,\%$ for 2006 data. Right: The phase diagram with data taken in 2007.

Pulsar	n_s
PSR J1538-5750	2.03
PSR J1905-0056	6.18
PSR J1158-5756	7.3
PSR J1845-0623	3.82
PSR J1703-4442	5.73
PSR J1703-4442	3.06

Table 6.3: The upper bounds on the signal n_s for a 95 % confidence belt. The first five pulsars are from the dataset with no cut. The last listing is from the dataset with energy and zenith angle cuts.

limit on the signal from neutrons with energies above 3 EeV will be derived in the next section.

6.1.3 Flux Limits

A flux limit, with a 95 % confidence level, can be derived for the signal from pulsar PSR J1703-4442. This is a flux limit for neutrons with energies above 3 EeV. This flux Φ is given by

$$\Phi = \frac{n_\mathrm{s}}{A_\mathrm{eff} T} \tag{6.1}$$

With T the time over which the data is collected, n_s the upper bound for the signal with a 95 % confidence level, and A_eff is the effective area. A_eff is given by

$$A_\mathrm{eff} = S(\theta, E)\bar{A} \tag{6.2}$$

With $S(\theta, E)$ the sensitivity function that is dependent on the energy E of the cosmic rays, and the zenith angle θ of the source. However for energies above 3 EeV the surface detector becomes fully sensitive, thus S is a function of θ only. The $\bar{A}$ in equation (6.2) is the mean area of the surface detector over period T. The sensitivity function of an object with known direction can be calculated. From the source direction, the effective area of the surface detector depends on the cosine of the angle between the vertical (at the detector) and the direction of the source i.e. the zenith angle of the object. Since the Earth is rotating θ changes with time. The $\cos(\theta)$ for an object with right ascension RA and declination Dec can be calculated if the local sidereal time LST is known.

$$\cos(\theta) = \cos(latt)\cos(Dec)\Big[\cos(RA)\cos(LST) + \sin(LST)\sin(RA)\Big] + \sin(Dec)\sin(latt) \tag{6.3}$$

With $latt$ the latitude of the Pierre Auger Observatory. One needs to calculate how the object travels through the sensitivity of the detector over one sidereal day, and make the comparison with an object that stays at full sensitivity over one sidereal day.

$$S(\theta) = \frac{\int_\mathrm{Tr} \cos(\theta(LST))dx}{\int_0^{2\pi} S_\mathrm{F} dx} = \frac{\int_\mathrm{Tr} \cos(\theta(LST))dx}{2\pi} \tag{6.4}$$

With dx an infinitesimal in the LST and $\int_\mathrm{Tr}$ is the integral over the range where $\cos(\theta) > 0.5$ ($\theta > 60°$). This is shown in figure 6.8. The value of $S(\theta)$ in this case is 0.364.

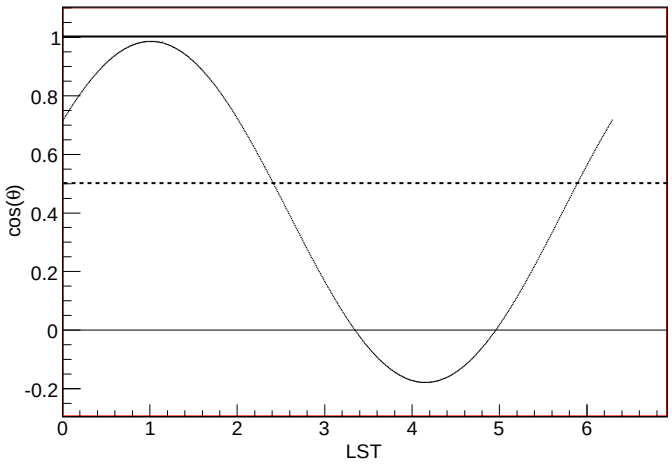

Figure 6.8: The fraction seen of the complete surface by an object with declination -44.42°. To calculate $S(\theta)$ the cosine function needs to be integrated above the dashed line and divided by total are between 0 and full line.

For the calculation of the mean area $\bar{A}$, the Auger energy spectrum [18] is used. This energy spectrum is shown if figure 6.9. From figure 6.9 the flux per particle can be calculated. Using the content of the first

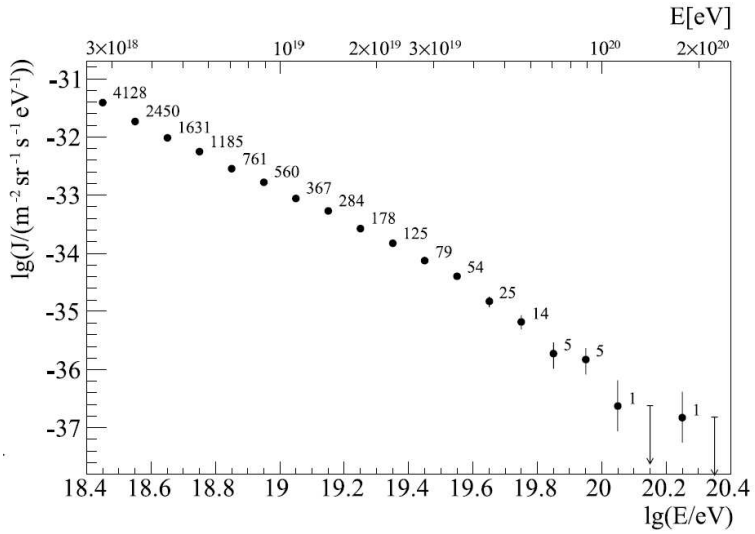

Figure 6.9: The Auger spectrum J as a function of energy, the vertical bars represent the statistical uncertainty. The systematic and the statistical uncertainties in the energy scale are of the order $\approx 22\,\%$ and $\approx 6\,\%$, respectively. The number at each data point is the number of events in that bin.

bin N_1 the flux per particle is given by

$$\frac{J_1 \Delta E_1}{N_1} \tag{6.5}$$

With J_1 the height of the spectrum in the first bin, and ΔE_1 the size of the first bin. The spectrum contains 20 bins and the ranges between $\log(E/eV)$=18.4 and 20.4, hence the size of the first bin is $\Delta E_1 = 6.5 \times 10^{17}\,\mathrm{eV}$. The total flux in the first bin is $J_1 = 10^{-31.4}\mathrm{m}^{-2}\mathrm{sr}^{-1}\mathrm{s}^{-1}$, thus the flux per particle becomes

$$\frac{J_1 \Delta E_1}{N_1} = \frac{2.6 \times 10^{14}}{4128}\mathrm{m}^{-2}\mathrm{sr}^{-1}\mathrm{s}^{-1} = 6.3 \times 10^{-18}\mathrm{m}^{-2}\mathrm{sr}^{-1}\mathrm{s}^{-1} \tag{6.6}$$

The total number of events in figure 6.9 is 11857, this results in a total flux above $E = 10^{18.4}\,\mathrm{eV}$ of $11857 \times 6.3 \times 10^{-18}\mathrm{m}^{-2}\mathrm{sr}^{-1}\mathrm{s}^{-1} = 7.4 \times 10^{-14}\,\mathrm{m}^{-2}\mathrm{sr}^{-1}\mathrm{s}^{-1}$. The effective area of the detector has to be multiplied with the cosine of the zenith angle, therefore the number of events one expects to see at a given

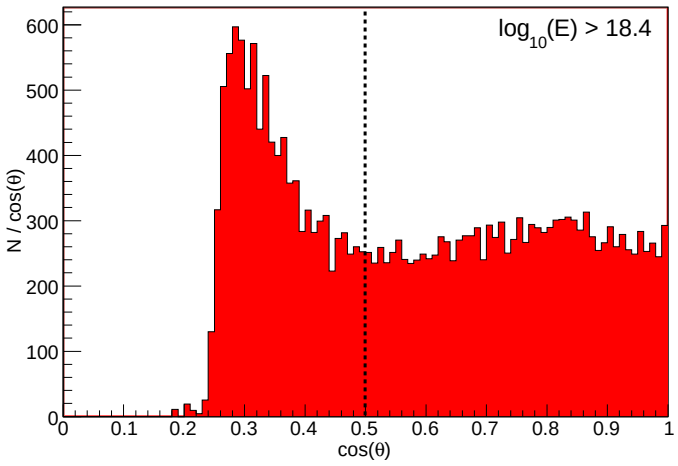

Figure 6.10: The distribution of zenith angle θ for all surface detector events between 1 January 2007 and 9 September 2007 with energy above $\log(E/\mathrm{eV}) = 18.4$. The number of events N in a bin, with size $\Delta\cos(\theta) = 0.01$, is divided by $\cos(\theta)$, if the detector is at full sensitivity this should result in a flat distribution. The dotted line gives the zenith angle cut $\theta < 60°$.

zenith angle should also behave like a cosine. In figure 6.10 the number of events N divided by $\cos(\theta)$ against $\cos(\theta)$ is plotted. At full sensitivity, this should give a flat distribution. This is indeed the case for $\cos(\theta) > 0.5$ (right from the dashed line). One bin, with size $\Delta\cos(\theta)$, in figure 6.10 corresponds to $2\pi\Delta\cos(\theta) = 2\pi \times 0.01\,\mathrm{sr}$. The average bin content for $\theta > 60°$ is 268.8 events. From the total flux over the complete sky (1 sr), the expected flux in one bin would be $2\pi \times 0.01 \times 7.4 \times 10^{-14} = 4.7 \times 10^{15}\,\mathrm{m^{-2}s^{-1}}$. If the number of events per bin, are divided by the flux per bin, the product $\bar{A}T$ becomes,

$$\bar{A}T = \frac{268.8}{4.7 \times 10^{15}} = 5.8 \times 10^{16}\,\mathrm{m^2\,s} \tag{6.7}$$

Using equations (6.2) and (6.1), combined with n_s=3.06 and $S(\theta, E)$=0.364, we find a flux limit on the signal from pulsar PSR J1703-4442 at a 95 % confidence level of

$$\Phi_\mathrm{s} = 1.4 \times 10^{-16}\,\mathrm{m^{-2}s^{-1}} \tag{6.8}$$

This flux limit, for neutrons with energies above 3 EeV, can be compared with the total flux from the pulsar at Earth. The energy flux $\Phi(d)$ from a pulsar at distance d, assuming that it emits all its energy in a cone with openings angle ρ, is given by

$$\Phi(d) = \frac{L}{2\pi d^2(1 - \cos(\rho))} \tag{6.9}$$

In which L is the luminosity of the pulsar. The angle ρ gives the angle between the magnetic axis and the boundary of the radio cone. This value of ρ is given by the empirical equation from [19]

$$\rho = 5°.75p^{-0.50} \tag{6.10}$$

When calculating the luminosity L, the energy loss of the pulsar derived from its slowdown rate $\dot{p}$ is used (equation (2.1)).

$$L = -\frac{dE}{dt} = \frac{8}{5}MR^2\frac{\pi^2}{p^3}\dot{p} \tag{6.11}$$

When combining equation (6.9) and (6.11) one obtains:

$$\Phi(d) = \frac{4\pi MR^2\dot{p}}{5d^2p^3(1 - cos(\rho))} \tag{6.12}$$

This would be the intensity of the beam at distance d. Using the assumptions that the radius of a pulsar R is 10 km and that its mass is M=1.4 $\mathrm{M_\odot}$, together with the information from the ATNF that p=1.7472 s, $\dot{p} = 1.4 \times 10^{-16}$ and $d = 5.34\,\mathrm{kpc}$, the total energy flux on Earth becomes.

$$\Phi(d) = 1.4 \times 10^3\,\mathrm{eV\,m^{-2}\,s^{-1}} \tag{6.13}$$

Assuming all this energy is emitted as neutrons of 3 EeV, one can calculate the maximum flux of high energy neutrons at Earth as:

$$\Phi_s = \frac{\Phi(d)}{E_{\min}} = 4.9 \times 10^{-16}\,\mathrm{m}^{-2}\mathrm{s}^{-1} \tag{6.14}$$

When comparing this number to the measured flux limit from equation (6.8) it can be concluded that less than 29 % of the pulsars energy loss is emitted as high energy neutrons.

6.2 *Final* Analysis

6.2.1 Pulsar Selection

A selection is made from the pulsars listed in the ATNF pulsar catalogue. Using the pulsar parameters obtained from this catalogue, and equation (4.26), the maximum number of bins can be calculated. A pulsar is selected when the resulting phase diagram contains more than 100 bins. In order to calculate the phase correctly, the first two time derivatives of the rotational frequency of the pulsar must be known. So pulsars for which $\dot{f}_0$ and $\ddot{f}_0$ are not given, are excluded. In this analysis, pulsars in binaries systems are excluded. Therefore, corrections on the arrival time due to binary orbits are not needed. In figure 6.11

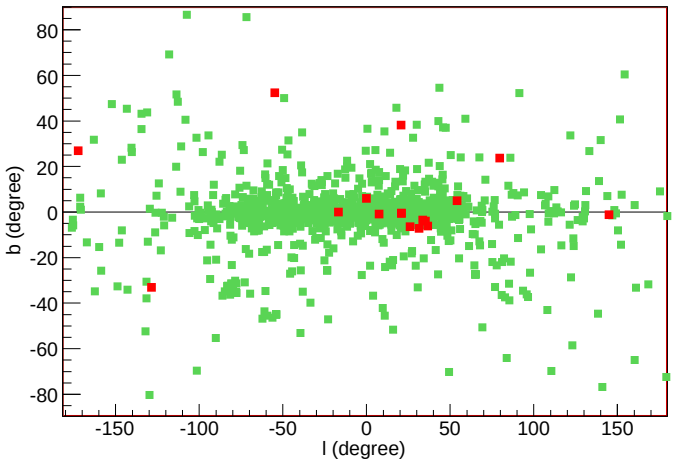

Figure 6.11: The pulsar population of all, non binary, pulsars is given in green squares. The selection of pulsars that are suitable for our method are given by the red squares.

the pulsar population, excluding binaries, is given in galactic coordinates. From the total of 1776 pulsars, 17 pulsars remain after applying the selection criterion (red squares). This corresponds to $\sim 0.96\,\%$ of the total pulsar population. From these 17 pulsars, there are 2 pulsars that are not in the field of view of the Pierre Auger Observatory. For the other 15 pulsars the parameters are give in table 6.2.1.

The periods of the selected pulsars are between 0.4 s and 7 s. The search strategy, described in section 3.2 is applied to the selected pulsars. All of the candidate sources are excluded when using a Q-value cut of 1 %.

name	RA (deg)	Dec (deg)	p_0 (s)	f_0 (Hz)	$\dot{f}_0$ (Hz s^{-1})	$\ddot{f}_0$ (Hz s^{-2})	t_0 (MJD)	w_{50} (ms)
B1828-11	277.7	-11.0	0.405043321630	2.46887171470	-3.658728E-13	8.72E-25	49621	3.2
J0725-1635	111.3	-16.6	0.4243114031834	2.356759664005	-5.1455E-16	1.5E-27	50884	4.1
B1756-22	269.9	-22.1	0.460974127869	2.16931914297	-5.11650E-14	-2.57E-25	49721	3.9
B1254-10	194.3	-10.5	0.6173076699955	1.6199377532557	-9.51798E-16	5.0E-28	49667	6.0
B1902-01	286.4	-0.9	0.643181259558	1.554771668389	-7.37678E-15	-1.96E-26	49721	6.2
B0329+54	53.2	54.6	0.714519699726	1.399541538720	-4.011970E-15	5.3E-28	46473	6.6
B1911-04	288.5	-4.7	0.825935803096	1.210747852620	-5.96334E-15	1.61E-26	46634	7.5
B1907+00	287.4	0.1	1.01694836198	0.98333409776	-5.33615E-15	1.7E-28	48740	8.0
B2044+15	311.7	15.7	1.1382856833155	0.8785140801273	-1.40711E-16	-1.1E-29	48742	9.6
B1848+12	282.8	13.0	1.20530328456	0.82966670116	-7.9297E-15	1.47E-25	49908	11
B1612+07	243.7	7.6	1.206801436397	0.828636733302	-1.620171E-15	-6.9E-28	49897	11.9
B1917+00	290.0	0.4	1.27226037471	0.786002629557	-4.73839E-15	1.66E-26	49427	10.1
B0751+32	118.7	32.5	1.442349479143	0.6933132465193	-5.19073E-16	-2.3E-28	48725	12.2
J1901-0906	285.5	-9.1	1.781927762343	0.5611899770197	-5.15952E-16	1.3E-27	50873	13
B1910+20	288.2	21.1	2.232969028273	0.4478342454993	-2.041156E-15	-2.67E-27	48740	9.9
B1753+52	268.6	52.0	2.39139679486	0.418165652037	-2.7351E-16	-5.2E-28	49666	11.4
J1830-1135	277.5	-11.6	6.2215526663	0.16073158159	-1.2336E-15	7.0E-26	51563	62.2

Table 6.4: Properties of the pulsars from the ATNF catalogue that result in phase diagrams

Chapter 7

Magnetars

7.1 *Initial* Analysis

The parameters of the magnetars are not as well knows as pulsar parameters. For example the pulse widths discussed in section 4.3 are not known. For the calculation of the number of bins in a phase diagram these values are required. But even when we make the assumption that the uncertainty on the calculated phase due to the pulse width is negligible, there are no magnetars that result in a phase diagram with more than 100 bins. The magnetar, for which a phase diagram with most bins (43) can be created is E 1841-045 (table 7.1). For this object phase diagrams have been created as described in section 3.2. The peak optimization is preformed on the data both with and without the energy and azimuth angle cuts.

The lowest value of Q that was obtained from the complete surface detector data set was $Q = 0.1$, this

E 1841-045	
p	11.77505416 s
f_0	0.0849252994 Hz
$\dot{f}_0$	-2.99681$\times 10^{-13}$ Hz s^{-1}
$\ddot{f}_0$	-
t_0	MJD 51618.0001

Table 7.1: Properties of candidate magnetar E 1841-045

is 10 times higher than the selection criterion described in section 3.2. For the high energy events, the lowest Q value was $Q = 0.3$. So for this magnetar the phase diagrams do not show any hints of periodicities.

7.2 *Final* Analysis

For the magnetar described in the previous section, the second order time derivative of the rotational frequency is not known (table 7.1). So it is not possible to calculate the phase with the method described in section 4.6.

Chapter 8

Conclusions and Discussion

In the previous sections we showed that a search for periodicity in the arrival times of cosmic rays can be performed on a limited sample of the known galactic pulsar population (15 pulsars). For these 15 pulsars, we have optimized search parameters using the surface detector data recorded in 2006. Afterwards, a search is performed on cosmic ray events originating from the direction of the pulsar using the surface detector data recorded in 2007. The analysis is performed once for all surface detector data, and once for events with an energy above 3 EeV and a zenith angle lower than 60°. In our results, there are no hints for the presence of the pulsars periods in the arrival times of the cosmic rays. More pulsars can be taken into account as soon as additional measurements on their rotational frequency f, and its time derivatives, $\dot{f}$ and $\ddot{f}$ are made. Especially the pulsars for which the fraction of the pulse width with respect to the pulsar period is less than 0.01, are interesting for this kind of analysis.
The magnetars are, from a theoretical point of view, good candidates for cosmic ray sources. However, only a few of these objects are known. For none of these magnetars the parameters are known well enough to analyze with our method. Additional measurements on the f, $\dot{f}$, and, $\ddot{f}$ are needed.
Initially, we neglected the time dependence of the pulsar period. The resulting selection of pulsars provided us with the possibility to develop our analysis. The number of pulsars that survived the initial selection was 65, whereas only 15 survived the final selection which took the time evolution of the pulsar period properly into account. Using the initial pulsar selection, the 2006 surface detector data resulted in five pulsar candidates, and one of these five was also selected in the high energy data set. We concluded that there was no significant signal present in the 2007 data using the same settings as in 2006. So we were able to derive an upper limit with a 95 % confidence level, on the signal in 2007 (table 8). If there had

Pulsar	n_s
PSR J1538-5750	2.03
PSR J1905-0056	6.18
PSR J1158-5756	7.3
PSR J1845-0623	3.82
PSR J1703-4442	5.73
PSR J1703-4442	3.06

Table 8.1: The upper bounds on the signal n_s for a 95 % confidence belt. The first five pulsars are from the dataset with no cut. The last listing is from the dataset with the cut.

been a significant signal present, in the complete data set, then it would most likely have to be a photon signal. This is because neutrons at low energies (below 1 EeV) would have decayed before reaching Earth. However, since the surface detector sensitivity to photons is still unknown, the derived upper limit can not be converted into a flux limit on the signal. For one pulsar (PSR J1703-4442), which is a candidate using the high energy data set from 2006, the flux limit on the signal is derived, as shown in section 6.1.3. The value of this 95 % confidence level upper limit is $\Phi_s = 1.4 \times 10^{-16}\,\mathrm{m^{-2}s^{-1}}$. When we compare this to a simple estimate of the energy flux at Earth originating from this pulsar it can be concluded that less than 29 % of the pulsars energy loss went into the signal.

Bibliography

[1] K. Greisen, Phys. Rev. Lett.**16**,748, (1966)

[2] G.T. Zatsepin & V.A. K'uzmin, Pis'ma Zh. Eksp. Teor. Fiz. **4**,114 (166)[JETP Lett. **4**,78 (1966)]

[3] The Pierre Auger Callaboration, Science, **vol. 318**, (9 Nov. 2007)

[4] A. Hewish, S.J. Bell, J.D.H. Pilkington, P.F. Scott and R.A. Collins, Nature **217**,709-713,(1968)

[5] J.R. Oppenheimer and G.M. Volkoff, Phys. Ref. **55**,374-381,(1939)

[6] M. Nagano and A.A. Watson, Rev. of Medern Pysics,**72**, No. 3, (2007)

[7] Nicolaus Copernicus, *De revolutionibus orbium coelestium*

[8] Copyright Wallace P.T, (2006).

[9] J. L. Han, Chin. J. Astron. Astrophys. Vol.6 (2006), **Suppl.2**,211-217.

[10] `http://www.atnf.csiro.au/research/pulsar/psrcat/`, Manchester,R.N.,Hobbs,G.B., Teoh, A.& Hobbs,M.,AJ,129,1993-2006(2005)

[11] Lyne A.G.,Mankelow S.H.,Bell J.H.,Manchester R.N,(2000),MNRAS.

[12] J. Albert *et al.* ApJ,**Vol. 669**(2007),1143-1149.

[13] Giller M, Lipski M,J. Phys. G:Nucl. Part. Phys. 28(2002) 1275-1286.

[14] Apeture calculation of the Pierre Auger Observatory surface detector, D. Allard [the Auger Collaboration],29^{th} ICRC 2005,**00**,101-106

[15] Scott M. Ransom,*et al. Science* 307, 892(2005).

[16] G.J. Feldman and R. D. Cousins, Physical Review D,**57**, p3873-p3889,(1998)

[17] The High Resolution Fly's Eye Collaboration. Observation of the Ankle and Evidence for a High-Energy Break in the Cosmic Ray Spectrum.

[18] Measurement of the UHECR energy spectrum using data from the Surface Detector of the Pierre Auger Observatory, Markus Roth [the Auger Collaboration], 30^{th} ICRC 2007.

[19] J.M. Rankin, Astrophysical Journal,**405**:285-297,(1993)